

The bathtub vortex in a rotating container

By **A. ANDERSEN**¹, **T. BOHR**², **B. STENUM**³
J. JUUL RASMUSSEN³ AND **B. LAUTRUP**⁴,

¹Cornell University, Dept. of Theoretical and Applied Mechanics, Ithaca, NY 14853, USA

²The Technical University of Denmark, Dept. of Physics, DK-2800 Kgs. Lyngby, Denmark

³Risø National Laboratory, Optics and Plasma Research Dept., DK-4000 Roskilde, Denmark

⁴The Niels Bohr Institute, Blegdamsvej 17, DK-2100 Copenhagen Ø, Denmark

(Received 12 June 2004)

We study the time-independent free surface flow which forms when a fluid drains out of a container, a so-called bathtub vortex. We focus on the bathtub vortex in a rotating container and describe the free surface shape and the complex flow-structure using photographs of the free surface, flow-visualizations, and velocity measurements. We find that the velocity field in the bulk of the fluid agrees with predictions from linear Ekman theory for the boundary layer at the bottom, and we describe the nonlinear features of the Ekman layer using averaged boundary layer equations. We introduce a radial expansion approximation of the central vortex core and reduce the model to a single 1st order equation. We solve the equation numerically and find that the axial velocity depends linearly on height whereas the azimuthal velocity is almost independent of height. We discuss the model of the bathtub vortex introduced by Lundgren (1985) and compare it with our experiment. We find that the measured velocities and surface profiles are well described by the model when Ekman up-flow and surface tension effects are included.

1. Introduction

Flows with a free surface are abundant in nature and technological applications and occur in, e.g., jets, rivers, and the oceans. The deformation of the free surface and the underlying flow are linked to each other, and intuitively one makes such a link when looking at, e.g., the small localized surface depressions on a river and associating them with vortex structures in the water. An important example of a vortex flow with a strongly deformed free surface is the so-called bathtub vortex, which forms when a fluid drains out of a container. We present an experimental and theoretical investigation of the bathtub vortex in a rotating flow. The experiment is carried out in a water filled cylindrical container rotating about its vertical axis of symmetry. At the center of the bottom of the container we have a small drain-hole and we establish a time-independent flow by recirculating the water through a rotationally symmetric inlet at the cylinder wall close to the bottom. In this source-sink flow an intense central vortex with localized axial down-flow is created and the free surface of the water above the drain-hole is strongly deformed and appears with a needle-like shape.

Bathtub vortex flows are familiar to most people, and since the free surface depression above the drain-hole makes the presence of the vortex easily visible, it is a beautiful example of a fluid vortex, see, e.g., the monograph by Lugt (1995). One would thus expect to find the phenomenon discussed in many fluid mechanics textbooks, but only very few theoretical discussions of bathtub vortex flows appear in the literature. Lamb (1945) describes a vortex with a free surface and models the flow as an outer line vortex with a viscous core, and similarly Feynman, Leighton & Sands (1965) present a simple ideal fluid model of the bathtub vortex. They, however, neglect the down-ward flow, and they do not take the kinematic boundary condition at the surface into account. Donaldson & Sullivan (1960) and Lewellen (1962) discuss classes of solutions of the Navier-Stokes

equations as models of bathtub vortex flows, but only for flows without a free surface. Einstein & Li (1951) model the bathtub vortex with a free surface, but they do not describe the interplay between the localized vorticity and the strong axial down-flow. In the following we focus on the time-independent bathtub vortex in a rotating container. We shall not discuss the central vortex in source-sink flows in non-rotating systems as investigated experimentally by Kawakubo et al. (1978) or the effect of the background rotation of the Earth on the direction of rotation of the bathtub vortex as discussed by Shapiro (1962) and Trefethen, Bilger, Fink, Luxton & Tanner (1965).

The flow-structure of the bathtub vortex in a rotating container is complex with several distinct flow regions. Based on our experimental observations we first discuss the flow qualitatively and present photographs of the free surface and flow-visualizations. Our goal in the paper is to provide basic theoretical understanding of the bathtub vortex in a rotating container, and to confront it with velocity and surface shape measurements. The central vortex core with localized axial down-flow is surrounded by a bulk region with a two-dimensional line vortex flow which is independent of height. At the container bottom an Ekman boundary layer is formed which gives rise to up-flow immediately outside the central region. We discuss the linear and the nonlinear properties of the Ekman boundary layer theoretically and compare the results with measurements.

The most fascinating feature of the bathtub vortex is the central needle-like surface depression and the associated vortex flow, which is also the most difficult aspect of the bathtub vortex to describe theoretically. We discuss and apply the method of Lundgren (1985) for describing the central free surface depression, and we find that numerical solutions of Lundgren's equations qualitatively have the same dependence on the rotation rate of the container as the measured surface profiles. We show that surface tension effects must be taken into account in a quantitative description of the experiment, and we

compare the measured surface and velocity profiles with numerical solutions of Lundgren's model with surface tension. A short presentation of some of our main results has appeared in Andersen, Bohr, Stenum, Juul Rasmussen & Lautrup (2003).

2. Experiment

2.1. *Experimental setup*

The present experiment was carried out in a cylindrical container on a rotating table. The setup is sketched in figure 1. The container consisted of a cylinder of radius 20 cm mounted inside a square reservoir container 5 mm above the plane horizontal bottom. Both the sides of the reservoir container and the cylinder were made of transparent perspex. A circular drain-hole of radius 1 mm was made in the 5 mm thick bottom metal plate at the center of the cylinder. The reservoir container was filled with water which seeped into the cylinder through the spacing between the bottom and the cylinder and flowed out through the drain-hole at the center. The water which left the drain-hole driven by gravity was pumped back into the reservoir, and the water level in the container was controlled by an overflow pipe in the reservoir outside the cylinder. A transparent perspex lid was placed on top of the cylinder several centimeters above the free surface to avoid contamination of the water. The container was rotated with a constant rotation rate about the vertical axis of symmetry of the cylinder. In this way a time-independent and rotationally symmetric free surface flow was established with a well-defined rotation rate of the container and a well-defined free surface height at the cylinder wall. The free surface shape and the velocity field of the time-independent flow were measured at rotation rates of 6 rpm, 12 rpm, and 18 rpm after a spin-up time of 20 min. The free surface height close to the cylinder wall was 10.9 cm in all three cases.

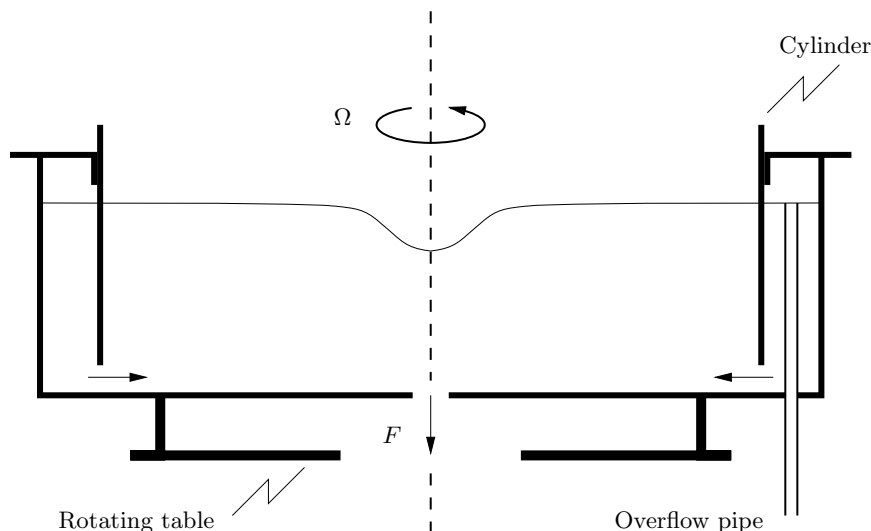


FIGURE 1. Apparatus (not to scale). The cylinder with radius 20 cm is mounted 5 mm above the bottom plate inside the square reservoir container which is filled with water. The container is placed on a table rotating with angular velocity Ω . The fluid which leaves the drain-hole with the flow-rate F is pumped back into the square container outside the cylinder. The overflow pipe outside the cylinder determines the unperturbed fluid depth.

2.2. Free surface

Figure 2 shows the observed profiles of the free surface for the time-independent flow at rotation rates of 6 rpm, 12 rpm, and 18 rpm. In the experiment we held the radius of the drain-hole and the unperturbed fluid depth constant, while we varied the rotation rate of the container. The depth of the dip in the free surface increases with increasing rotation rate, whereas the radius of the central region, where the dip is very distinct, is almost unaltered. In preliminary measurements with a fixed unperturbed fluid depth we observed that the depth of the central depression depended sensitively on the radius of the drain-hole and less on the rotation rate of the container. The outflow is driven by gravity and the flow-rate through the drain-hole is thus approximately constant when both the unperturbed fluid depth and the radius of the drain-hole are kept constant. A straight forward application of Torricelli's theorem (see, e.g., Batchelor (1967)) overestimates the

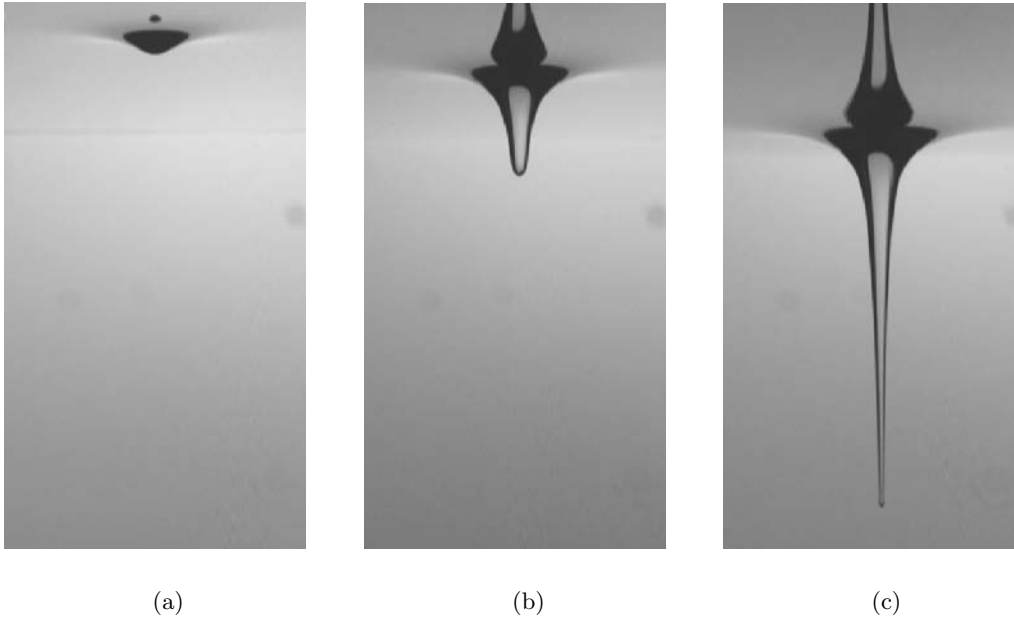


FIGURE 2. The free surface dip depends sensitively on the rotation rate of the container as shown in the photographs. Picture (a) was taken at 6 rpm, (b) at 12 rpm, and (c) at 18 rpm. In each photograph the area is 4.0 cm (horizontally) \times 7.2 cm (vertically) and the lower edge of the frame is 4.2 cm above the drain-hole. The structure above the surface is due to reflections. measured flow-rate by 20 % when the container is not rotating. The measured flow-rate decreases by approximately 15 % when the rotation rate is increased from 6 rpm to 18 rpm. The flow-rate measurements are summarized in table 1 in § 3.3.

2.3. Tip instability

The tip of the free surface dip is stable when the rotation rate of the container is below a certain value. At higher rotation rates the dip is deeper and the tip oscillates vertically, and at even higher rotation rates air-bubbles detach from the tip as shown in figure 3. Initially the bubbles are not spherical but appear elongated. Further downstream they obtain an almost spherical shape. Around the critical value of the rotation rate (which is approximately 22 rpm) the tip appears almost like a cylinder of air surrounded by rapidly spinning water. The radius of the air cylinder is about 0.5 mm and surface tension gives



FIGURE 3. The tip of the surface depression is unstable when the rotation rate of the container is high. An air-bubble with radius of about 0.5 mm has just detached from the tip and is dragged down the drain by the surrounding flow. The photograph was made with a preliminary setup.

rise to the bubble-forming instability at the tip. When the rotation rate of the container is increased further, the frequency of bubble shedding increases until the air-filled core extends all the way down through the drain-hole.

2.4. *Flow-structure*

Figures 4 and 5 show flow visualizations made at 12 rpm by illuminating a vertical cross-section through the axis of symmetry and then adding fluorescent dye at the surface (figure 4) or at the bottom inlet (figure 5). The fluorescent dye was only visible when illuminated by the vertical light sheet created using a slide projector with a thin metal plate with a slit in front of it.

Figure 4 shows the down-flow above the drain-hole. The dye was added at the surface



FIGURE 4. Visualization of the downward flow in the vortex core above the drain-hole at 12 rpm. The dye was added at the surface and is flowing in a free surface boundary layer to the core region where it flows rapidly down-ward to the drain-hole. The top part of the image shows reflections in the free surface which are artifacts of the method of observation.

at a distance from the center and is flowing toward the center in a thin surface boundary layer. The small free surface dip (see also figure 2(b)) is visible above the central localized down-flow region which appears like a “drainpipe” with radius comparable to that of the drain-hole. The free surface boundary layer carries only a small fraction of the total flow-rate, and most of the inflow takes place in the bottom boundary layer.

The photographs in figure 5 show a time-series of visualizations using dye added at the bottom inlet. Outside the up-flow region seen in figure 5, the flow is controlled by the rotation of the container. The bottom boundary layer has the characteristics of an Ekman layer and the Taylor-Proudman theorem applies to the geostrophic flow above it (see, e.g., Batchelor (1967)). The thickness of the bottom boundary layer is therefore almost constant and the flow above it essentially two-dimensional and independent of height. At 12 rpm the Ekman layer thickness is about 1 mm. The thin bottom layer is visible to the left in figure 5(a) and immediately to the right of the drain-hole in figure 5(b). The blob of dye spirals up-ward around the axis of symmetry and as in a Poincaré section forms the layered structure in figure 5(c) – (f) which surrounds the down-flow “drainpipe” from the free surface layer. We note that a similar up-flow was visualized by Lewellen (1962) close to the drain-hole in a rotating flow without a free surface. The mechanism which creates the up-flow is similar to Ekman pumping. However, the standard linear description of Ekman layers is not valid in this region and the nonlinear terms in the Navier-Stokes equations must be included to model the bottom boundary layer close to the drain-hole. We discuss the Ekman layer further in § 3 and § 4.

Figure 6 shows the long path followed by a small tracer particle which spirals up-ward from the Ekman layer and then down toward the drain-hole. The recording was made with a vertical light sheet as in the flow visualizations and the trajectory was identified using particle tracking software (DigImage, University of Cambridge, UK).

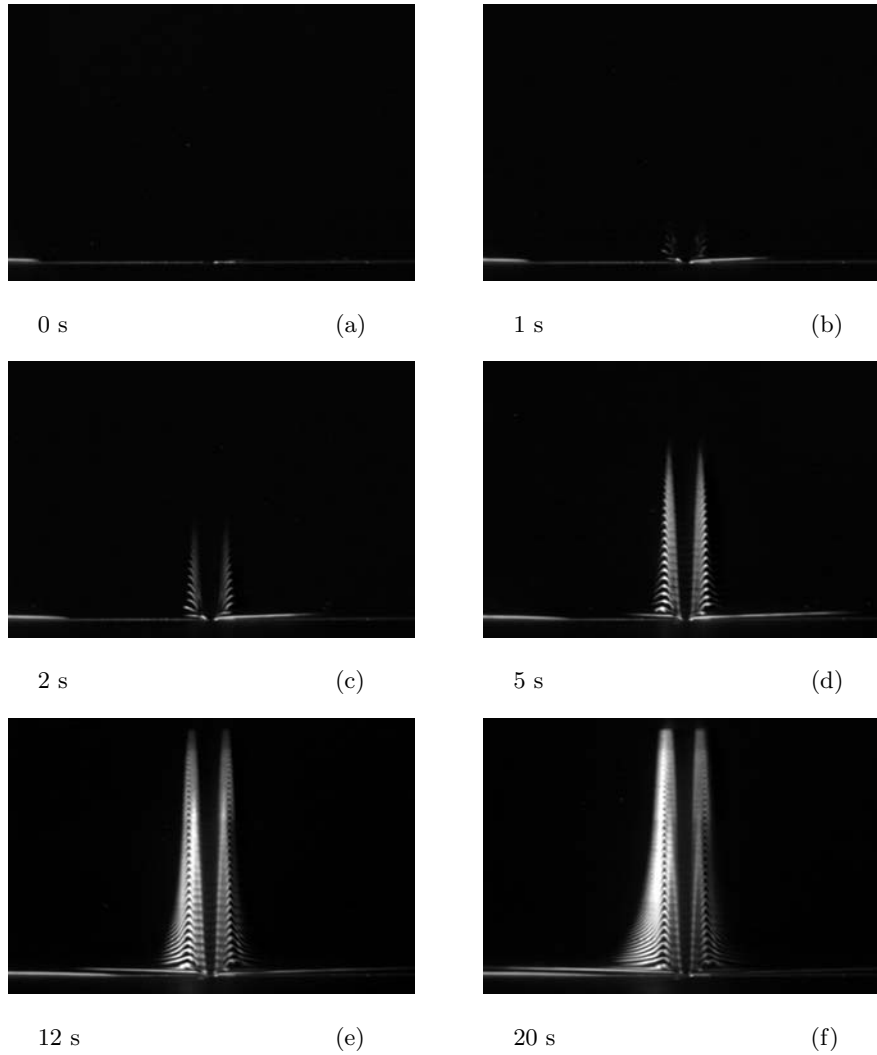


FIGURE 5. Visualization of the flow in the bottom boundary layer and the central up-flow around the drain-hole at 12 rpm. The images are 7.8 cm (horizontally) \times 5.4 cm (vertically) with the bottom visible as the thin bright line. The bottom Ekman boundary layer is about 1 mm thick and initially visible to the left of the drain-hole in (a). Subsequently, some of the dye from the Ekman layer spirals up-ward around the axis of symmetry until the flow turns and the dye spirals down toward the drain-hole.

Figure 7 summarizes our qualitative description of the flow-structure of the bathtub vortex and shows a sketch of the cross section through the spiraling streamlines.

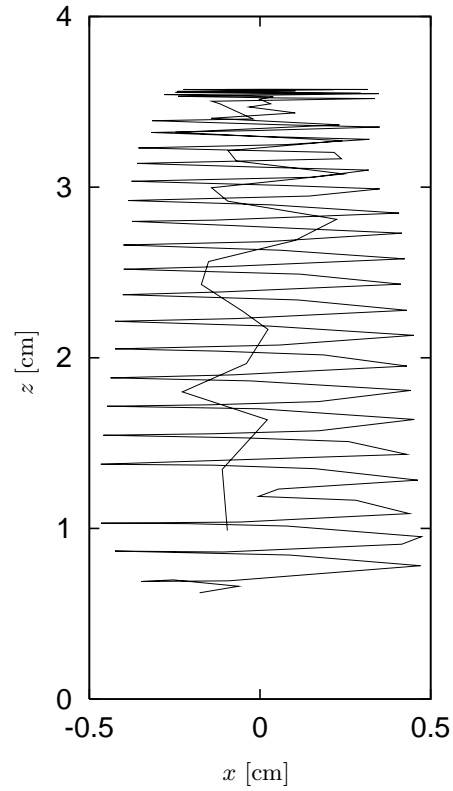


FIGURE 6. The trajectory of a tracer particle at 6 rpm. The tracer particle spirals up-ward in the next-to-central upwelling region at a distance between 4 mm and 5 mm from the center until it turns at a height of 3.6 cm above the bottom and spirals down toward the drain-hole with increasing vertical velocity.

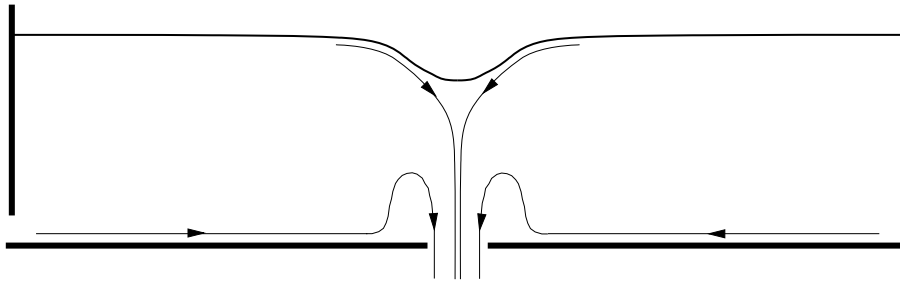


FIGURE 7. The sketch shows the characteristic flow-regions of the bathtub vortex. The main part of the radial in-flow is carried by the bottom Ekman boundary layer, and the next-to-central up-welling region surrounds the central drainpipe from the free surface above the drain-hole.

3. Linear Ekman theory for the bottom boundary layer

3.1. Governing equations

The Navier-Stokes equations and the continuity equation for a time-independent and incompressible flow in the reference frame co-rotating with the container are

$$(\mathbf{u} \cdot \nabla)\mathbf{u} = -\frac{1}{\rho} \nabla p + \nu \nabla^2 \mathbf{u} - 2\boldsymbol{\Omega} \times \mathbf{u} , \quad (3.1)$$

$$\nabla \cdot \mathbf{u} = 0 , \quad (3.2)$$

where \mathbf{u} is the velocity in the co-rotating reference frame, p the effective pressure which includes a gravitational and a centrifugal term, $\boldsymbol{\Omega}$ the angular velocity of the container, ρ the fluid density, and ν the kinematic viscosity.

The characteristic value of the ratio between the nonlinear term and the Coriolis term is the Rossby number, Ro , and the characteristic value of the ratio between the viscous term and the Coriolis term is the Ekman number, Ek . We use the definitions

$$\text{Ro} = \frac{U}{2\Omega L} , \quad (3.3)$$

$$\text{Ek} = \frac{\nu}{2\Omega L^2} , \quad (3.4)$$

where L is the characteristic length scale and U is the characteristic velocity scale. In linear Ekman theory the Rossby number is assumed to be small, and thus the nonlinear terms in the Navier-Stokes equations are neglected.

3.2. Linear Ekman theory for source-sink flows

The flow has rotational symmetry and we therefore use polar coordinates (r, θ, z) with corresponding velocity components (u, v, w) . Similar to standard boundary layer theory

only the derivatives with respect to z are kept in the viscous terms, and the Navier-Stokes equations (3.1) thus reduce to

$$0 = -\frac{1}{\rho} \frac{\partial p}{\partial r} + \nu \frac{\partial^2 u}{\partial z^2} + 2\Omega v, \quad (3.5)$$

$$0 = \nu \frac{\partial^2 v}{\partial z^2} - 2\Omega u, \quad (3.6)$$

$$0 = -\frac{1}{\rho} \frac{\partial p}{\partial z}. \quad (3.7)$$

Since it is assumed that the vertical velocities are small it follows from the axial Navier-Stokes equation (3.7) that the pressure is independent of z and that the pressure gradient $\partial p/\partial r$ therefore is equal to its value in the geostrophic bulk where the pressure gradient and the Coriolis force balance each other. The governing equations thus reduce to the following set of coupled linear ordinary differential equations

$$0 = \nu \frac{\partial^2 u}{\partial z^2} + 2\Omega (v - v_0), \quad (3.8)$$

$$0 = \nu \frac{\partial^2 v}{\partial z^2} - 2\Omega u, \quad (3.9)$$

where v_0 is the azimuthal velocity in the geostrophic bulk. The general solution of the Ekman equations (3.8) and (3.9) is discussed, e.g., by Batchelor (1967). With the boundary conditions $u(r, z) = v(r, z) = 0$ at $z = 0$, $u(r, z) \rightarrow 0$ as $z \rightarrow \infty$, and $v(r, z) \rightarrow v_0(r)$ as $z \rightarrow \infty$, the equations have the solution:

$$u(r, z) = -v_0(r) e^{-z/\delta} \sin(z/\delta), \quad (3.10)$$

$$v(r, z) = v_0(r) [1 - e^{-z/\delta} \cos(z/\delta)], \quad (3.11)$$

where the Ekman boundary layer thickness is defined as

$$\delta = \sqrt{\frac{\nu}{\Omega}} . \quad (3.12)$$

The thickness of the Ekman layer is thus constant in the linear approximation. The continuity equation (3.2) relates u and w in the following way

$$\frac{1}{r} \frac{\partial(ru)}{\partial r} + \frac{\partial w}{\partial z} = 0 , \quad (3.13)$$

and since $w(r, z) = 0$ for $z = 0$, it follows that

$$\begin{aligned} w(r, z) &= \frac{1}{r} \frac{d(rv_0)}{dr} \int_0^z ds e^{-s/\delta} \sin(s/\delta) \\ &= \frac{\delta}{2r} \frac{d(rv_0)}{dr} \left(1 - e^{-z/\delta} [\sin(z/\delta) + \cos(z/\delta)] \right) . \end{aligned} \quad (3.14)$$

In the geostrophic bulk the vertical velocity component is therefore proportional to the z -component of the vorticity ω_z :

$$w_0 = \frac{\delta}{2r} \frac{d(rv_0)}{dr} = \frac{\delta}{2} \omega_z . \quad (3.15)$$

A vortex with positive vorticity thus gives rise to Ekman pumping (up-flow) whereas a vortex with negative vorticity produces Ekman suction (down-flow).

The bathtub vortex flow outside the central vortex core, i.e., in the geostrophic bulk, can be modeled as a line vortex flow with circulation Γ :

$$v_0(r) = \frac{\Gamma}{2\pi r} . \quad (3.16)$$

It follows from equation (3.14) that $w = 0$ in this particular solution since the flow is irrotational. The up-flow vanishes outside the central core because of the boundary conditions at the free surface. The free surface is almost horizontal outside the vortex

core and because of the kinematic boundary condition we have $w = 0$ at the surface. The circulation is related to the flow rate, F , which we define as the following integral

$$F \equiv - \int_0^\infty dz 2 \pi r u = \frac{\Gamma \delta}{2} . \quad (3.17)$$

A particular solution of (3.8) and (3.9) modeling the bathtub vortex is therefore

$$u = - \frac{F}{\pi \delta r} e^{-z/\delta} \sin(z/\delta) , \quad (3.18)$$

$$v = \frac{F}{\pi \delta r} [1 - e^{-z/\delta} \cos(z/\delta)] , \quad (3.19)$$

$$w = 0 . \quad (3.20)$$

Outside the vortex core in the bulk of the fluid far above the Ekman layer we thus expect that $u \approx 0$ and $v \approx F/(\pi \delta r)$ because of the special structure of the linear Ekman solution. Similar results were derived and confirmed experimentally for a source-sink flow without a free surface by Mory & Yurchenko (1993).

3.3. Measured azimuthal velocity profiles

Figure 8 shows the azimuthal velocity profile measured at 6 rpm in the bulk of the fluid 5.7 cm above the bottom. The flow outside the central region is that of a line vortex and at the cylinder wall a vertical boundary layer is formed. We measured similar velocity profiles at 12 rpm and 18 rpm. Table 1 summarizes the measurements of the azimuthal velocities in the bulk of the fluid at 6 rpm, 12 rpm, and 18 rpm and shows the measured total flow-rate and the calculated Ekman layer thickness. In the calculations we used the kinematic viscosity of water $\nu = 0.0089 \text{ cm}^2 \text{ s}^{-1}$ at 25 °C, see Kaye & Laby (1973). The measured azimuthal velocities in the bulk are modeled well by the line vortex $v_0 = F/(\pi \delta r)$, and the theoretical values agree with the measured vortex strengths to within 5 – 10%. The experiment thus confirms the prediction of linear Ekman theory.

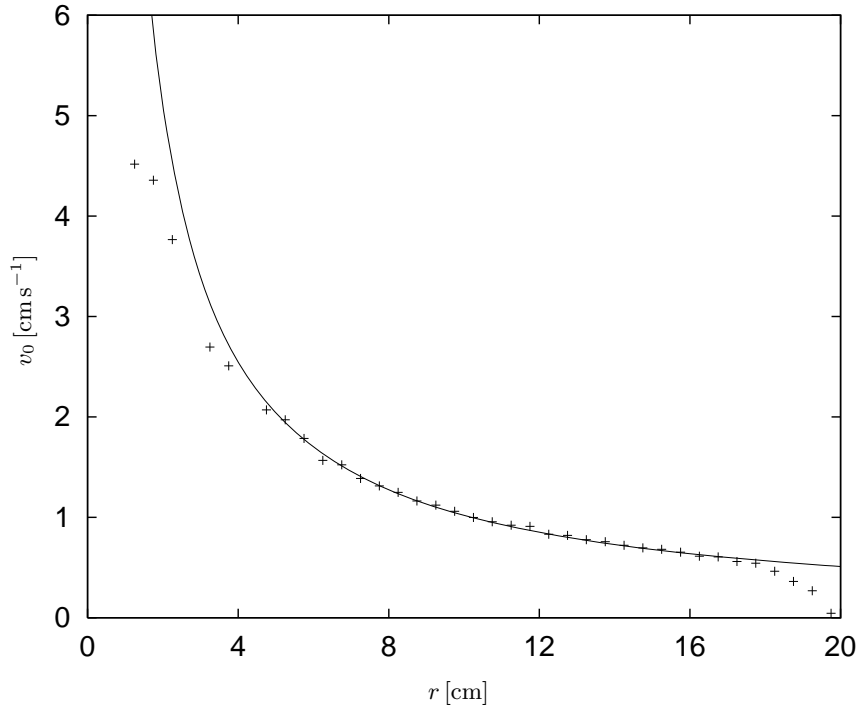


FIGURE 8. The azimuthal velocity profile measured at 6 rpm using particle tracking with a horizontal light sheet and the best fit of a line vortex A/r to the experimental data. The plus signs show the measurements and the solid curve is the best fit in the range $5 \text{ cm} \leq r \leq 15 \text{ cm}$. The vertical Stewartson boundary layer at the cylinder wall is about 1 cm thick.

The vertical Stewartson boundary layer at the cylinder wall is much thicker than the bottom Ekman layer. Following Greenspan (1968) we estimate that the thickness of the Stewartson layer is $L \text{Ek}^{1/4} \approx 1 \text{ cm}$, where the Ekman number is defined in equation (3.4) and where we use the radius of the container $L = 20 \text{ cm}$ as the characteristic length scale. The estimated boundary layer thickness agrees with the results shown in figure 8.

3.4. *Validity of the linear Ekman solution*

The linear Ekman layer approximation (3.8) and (3.9) is only valid when the flow relative to the background rotation is weak and the nonlinear terms in the Navier-Stokes

$\Omega/2\pi$ [rpm]	F [cm^3s^{-1}]	δ [mm]	$F/\pi\delta$ [cm^2s^{-1}]	A [cm^2s^{-1}]
6	3.62	1.190	9.7	10.2
12	3.54	0.842	13.4	14.2
18	3.16	0.687	14.6	16.0

TABLE 1. The measured flow rate, F , the thickness of the Ekman layer, $\delta = \sqrt{\nu/\Omega}$, and the vortex strength predicted from linear Ekman theory, $F/(\pi\delta)$, for different values of the angular velocity, Ω . The 5th column shows the values of A obtained from fits of the line vortex A/r to the measured azimuthal velocity profiles in the range $5 \text{ cm} \leq r \leq 15 \text{ cm}$. The theoretical predictions of the vortex strengths $F/(\pi\delta)$ agree with the measured values of A to within 5 – 10 %.

equations are negligible, i.e., when the Rossby number (3.3) and the Ekman number (3.4) are small:

$$\text{Ro} \ll 1 \quad \text{and} \quad \text{Ek} \ll 1 . \quad (3.21)$$

We therefore estimate the local Rossby number and the local Ekman number:

$$\text{Ro} = \frac{F}{2\pi\sqrt{\nu\Omega}r^2} , \quad (3.22)$$

$$\text{Ek} = \frac{\nu}{2\Omega r^2} , \quad (3.23)$$

where we use $U \approx F/(\pi\delta r)$ and $L \approx r$. At 12 rpm we find the estimates

$$\text{Ro} \approx 1 \quad \text{when} \quad r \approx 2 \text{ cm} , \quad (3.24)$$

$$\text{Ek} \approx 1 \quad \text{when} \quad r \approx 0.06 \text{ cm} . \quad (3.25)$$

The nonlinear terms are therefore important in the bathtub vortex experiment at small

values of r whereas they can be neglected when modeling the flow outside the central vortex core as in the linear Ekman boundary layer analysis in § 3.3.

4. Nonlinear properties of the Ekman layer

4.1. Averaged boundary layer equations

The nonlinear terms make it impossible to solve the boundary layer equations for the bottom Ekman layer analytically. We therefore investigate the nonlinear effects on the Ekman up-flow and the boundary layer thickness by deriving averaged boundary layer equations and obtaining approximate solutions to the governing equations. The averaged boundary layer equations do not describe the down-flow above the drain-hole but only the up-flow caused by the bottom boundary layer and the effect of the nonlinear terms on the boundary layer thickness and the up-flow velocity outside the vortex core.

We use a standard boundary layer approximation of the radial and the azimuthal Navier-Stokes equations in which we keep the nonlinear terms but neglect the radial derivatives in the viscous terms and set the pressure equal to its value in the bulk

$$u \frac{\partial u}{\partial r} + w \frac{\partial u}{\partial z} - \frac{v^2 - v_0^2}{r} = \nu \frac{\partial^2 u}{\partial z^2} + 2\Omega(v - v_0) , \quad (4.1)$$

$$u \frac{\partial v}{\partial r} + w \frac{\partial v}{\partial z} + \frac{uv}{r} = \nu \frac{\partial^2 v}{\partial z^2} - 2\Omega u , \quad (4.2)$$

where $v(r, z) \rightarrow v_0(r)$ as $z \rightarrow \infty$. Owen, Pincombe & Rogers (1985) analyzed these equations using an averaging method similar to the technique introduced by von Kármán (1921) and Pohlhausen (1921). The authors applied a self-similar boundary layer profile which is described by a single length scale. Therefore the approximate solution has the same damped oscillatory structure as the solution to the linear Ekman equations but with a boundary layer thickness which depends on the local Rossby number. Andersen,

Lautrup & Bohr (2003) introduced a non self-similar profile which describe the decay and the oscillations in the boundary layer by two different length scales and showed that the model for vortex flows with a rigidly rotating core performs markedly better than the model based on the self-similar profile.

In the following we use the non self-similar profile which is a generalization of the solution (3.10) and (3.11) of the linear Ekman equations

$$u(r, z) = -v_0 e^{-z/\delta_1} \sin(z/\delta_2) , \quad (4.3)$$

$$v(r, z) = v_0 [1 - e^{-z/\delta_1} \cos(z/\delta_2)] , \quad (4.4)$$

where v_0 , δ_1 , and δ_2 are functions of r . The two length scales δ_1 and δ_2 describe respectively the decay and the oscillations in the boundary layer structure. We have $\delta_1 = \delta_2 = \sqrt{\nu/\Omega}$ when the local Rossby number is small, but in general the two length scales are different. We integrate the governing equations (4.1) and (4.2) with respect to z from zero to infinity, and the resulting averaged equations become

$$\frac{1}{r} \frac{d(rv_0^2 K_2)}{dr} + \frac{v_0^2}{r} (2K_4 - K_5) = \frac{\nu v_0}{\delta_2} - 2\Omega v_0 K_4 , \quad (4.5)$$

$$\frac{1}{r^2} \frac{d(r^2 v_0^2 K_3)}{dr} - \frac{v_0 K_1}{r} \frac{d(rv_0)}{dr} = -\frac{\nu v_0}{\delta_1} + 2\Omega v_0 K_1 , \quad (4.6)$$

where we define

$$K_1 = 4K_3 = \frac{\delta_1^2 \delta_2}{\delta_1^2 + \delta_2^2} , \quad K_2 = \frac{\delta_1^3}{4(\delta_1^2 + \delta_2^2)} , \quad (4.7)$$

$$K_4 = \frac{\delta_1 \delta_2^2}{\delta_1^2 + \delta_2^2} , \quad K_5 = K_2 + \frac{1}{2} K_4 . \quad (4.8)$$

The two differential equations involve the three functions δ_1 , δ_2 , and v_0 . To complete

the model we use the top boundary condition to either specify the up-flow, as in linear Ekman theory, or to specify the azimuthal velocity in the bulk of the fluid.

4.2. *The nonlinear Ekman layer for the bathtub vortex*

The averaged equations do not allow us to model the up-flow profile immediately outside the vortex core in detail, since they only describe the effect of the bottom boundary and do not take the structure of the down-flow above the drain-hole into account. We therefore only investigate the qualitative effects of the nonlinearities on the boundary layer thickness and the up-flow. For simplicity we assume that the azimuthal velocity in the bulk of the fluid has the following form

$$v_0(r) = \frac{F}{\pi \sqrt{\nu/\Omega} r} \left[1 - \exp\left(-\frac{r^2}{\xi^2}\right) \right], \quad (4.9)$$

where ξ is the radius of the vortex core. The velocity profile matches the outer line vortex (3.16) and describes a vortex core with solid body rotation. We note that in this case linear Ekman theory (3.15) predicts the Gaussian up-flow profile

$$w_0(r) = \frac{F}{\pi \xi^2} \exp\left(-\frac{r^2}{\xi^2}\right), \quad (4.10)$$

whereas the expression for Ekman pumping in the averaging model generalizes to

$$w_0(r) = \frac{1}{r} \frac{d(K_1 r v_0)}{dr}. \quad (4.11)$$

We solve the averaged equations numerically using the functions $\alpha \equiv K_1$ and $\beta \equiv \delta_1/\delta_2$ and rewrite equations (4.5) and (4.6) as

$$\alpha' = \frac{2}{v_0} \left[\left(v_0' + \frac{v_0}{r} + 4\Omega \right) \alpha - \frac{2\nu}{\delta_1} \right], \quad (4.12)$$

$$\beta' = -\frac{2}{\alpha v_0} \left[\left(2v_0' + \frac{v_0}{r} + 4\Omega \right) \alpha\beta + \left(\frac{3v_0}{r} + 4\Omega \right) \frac{\alpha}{\beta} - \frac{4\nu}{\delta_2} \right], \quad (4.13)$$

where the prime denotes differentiation with respect to r . The functions δ_1 and δ_2 are expressed in terms of α and β in the following way

$$\delta_1 = \alpha \left(\beta + \frac{1}{\beta} \right), \quad \delta_2 = \alpha \left(1 + \frac{1}{\beta^2} \right). \quad (4.14)$$

We supplement the equations by boundary conditions at large $r = L$:

$$\alpha(L) = \frac{1}{2} \sqrt{\frac{\nu}{\Omega}}, \quad \beta(L) = 1. \quad (4.15)$$

Figure 9 shows a numerical solution of the averaged boundary layer equations (4.12) and (4.13) at 12 rpm. The nonlinearities give rise to a weaker central up-flow and a decrease in the boundary layer thickness with δ_2 always being less than δ_1 . The nonlinear effects are pronounced in the vortex core where the local Rossby number is greater than 1. Notice the cross-over between the azimuthal vortex velocity (solid line) and the solid body rotation of the container (dashed line) shown in figure 9.

5. Drainpipe model

Both the azimuthal and the vertical velocities are high in the central down-flow region compared with the bulk flow velocities, and the flow below the surface dip is an intense vortex with axial flow localized to a weakly conical region with radius comparable to the radius of the drain-hole as visualized in figure 4. To model the drainpipe below the surface dip we assume that the downward flow has a parabolic profile, and we make a radial expansion of the velocity components and the pressure. We assume that the expansion is valid in the viscous vortex core and we obtain a closed system of coupled ordinary differential equations by matching the inner solution to the height independent

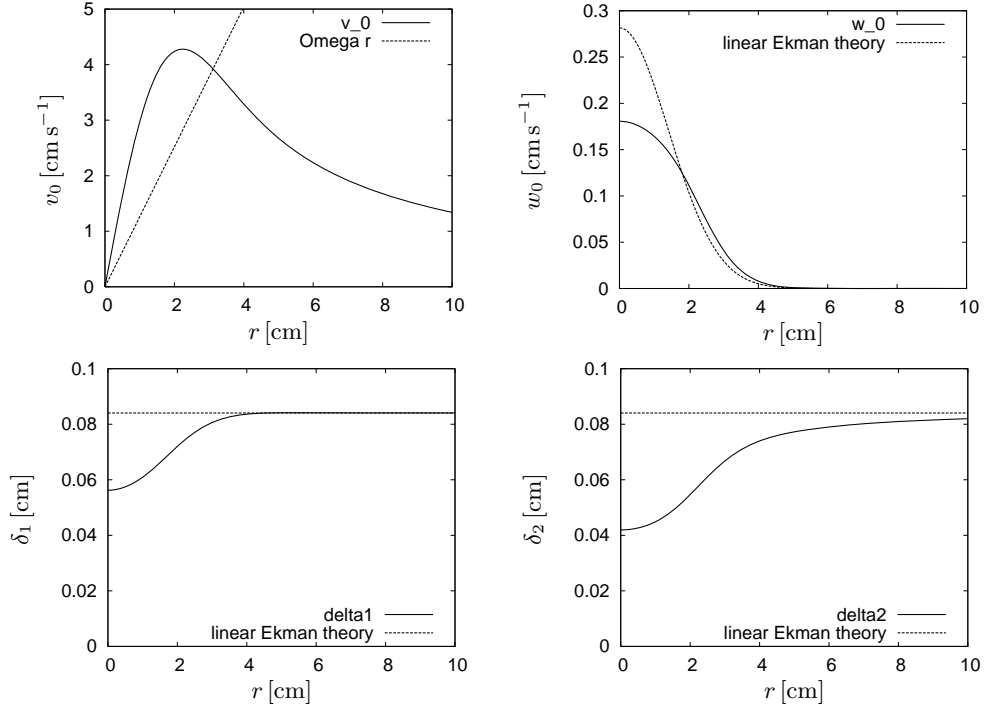


FIGURE 9. Numerical solution (solid lines) of the averaged boundary layer equations (4.12) and (4.13) at 12 rpm with the azimuthal velocity profile (4.9) and the parameters $F = 3.54 \text{ cm}^3 \text{ s}^{-1}$, $\nu = 0.0089 \text{ cm}^2 \text{ s}^{-1}$, and $\xi = 2.0 \text{ cm}$. For comparison we plot the solid body rotation of the container, Ωr , and the linear Ekman theory (3.12) and (4.10) using the dashed lines.

line vortex outside the vortex core. We reduce the problem to a single 1st order differential equation and describe a numerical solution modeling the bathtub vortex.

5.1. Vertical boundary layer approximation

The downward velocity with which the fluid leaves the drain-hole is an important scale for the velocity field in the central region of the bathtub vortex. In the following we use W to denote the characteristic value of the downward velocity, Ω_C to denote the central rotation rate, and H to denote the unperturbed fluid depth. The central azimuthal velocities are large compared with the radial velocities, and we therefore approximate

the radial Navier-Stokes equation using a vertical boundary layer approximation. The approximation is valid if the assumption of a small central Rossby number is satisfied

$$\text{Ro}_C = \frac{W}{H\Omega_C} \ll 1. \quad (5.1)$$

We estimate Ω_C and Ro_C by matching the line vortex flow (3.16) to a rigidly rotating vortex core with radius, R , equal to the radius of the drain-hole. The estimate gives

$$\Omega_C \approx \frac{F}{\pi\sqrt{\nu/\Omega}R^2}. \quad (5.2)$$

We find $\Omega_C \approx 10^4$ rpm and $\text{Ro}_C \approx 0.01$ using the measured value of the circulation at 12 rpm, and we therefore estimate that the assumption (5.1) is satisfied. The vertical boundary layer approximation of the central region of the bathtub vortex is

$$\frac{v^2}{r} = \frac{1}{\rho} \frac{\partial p}{\partial r}, \quad (5.3)$$

$$u \frac{\partial v}{\partial r} + w \frac{\partial v}{\partial z} + \frac{uv}{r} = \nu \left(\frac{\partial^2 v}{\partial r^2} + \frac{1}{r} \frac{\partial v}{\partial r} - \frac{v}{r^2} \right), \quad (5.4)$$

$$u \frac{\partial w}{\partial r} + w \frac{\partial w}{\partial z} = -\frac{1}{\rho} \frac{\partial p}{\partial z} + \nu \left(\frac{\partial^2 w}{\partial r^2} + \frac{1}{r} \frac{\partial w}{\partial r} \right) - g, \quad (5.5)$$

and in addition we have the continuity equation

$$\frac{1}{r} \frac{\partial(ru)}{\partial r} + \frac{\partial w}{\partial z} = 0. \quad (5.6)$$

Here and in § 6 we write the Navier-Stokes equations in the laboratory reference frame, and we use p to denote the pressure and not the effective pressure as in § 3 and § 4.

5.2. Radial expansion

We assume that the downward flow has a parabolic profile, and in the following we expand the velocity and the pressure in powers of r . We write the expansion of w using

the functions $a(z)$ and $b(z)$, the expansion of v using the functions $\Omega_1(z)$ and $\Omega_3(z)$, and the expansion of p using the functions $p_0(z)$ and $p_2(z)$:

$$u(r, z) = \frac{1}{2} a'(z) r - \frac{1}{4} b'(z) r^3, \quad (5.7)$$

$$v(r, z) = \Omega_1(z) r + \Omega_3(z) r^3, \quad (5.8)$$

$$w(r, z) = -a(z) + b(z) r^2, \quad (5.9)$$

$$p(r, z) = \rho [p_0(z) + p_2(z) r^2], \quad (5.10)$$

where the expression for u follows from the continuity equation. Using the boundary layer equations (5.3) – (5.5) we obtain to lowest order in r the following

$$\Omega_1^2 = 2 p_2, \quad (5.11)$$

$$\Omega_1 a' - a \Omega_1' = 8 \nu \Omega_3, \quad (5.12)$$

$$a a' = -p_0' + 4 \nu b - g, \quad (5.13)$$

where the prime denotes differentiation with respect to z . These equations for the central vortex core are similar to the equations applied by Eggers & Brenner (2000) to model a spinning jet and the nonlinear properties of its break-up into droplets. For a free jet the system of equations are supplemented by boundary conditions at the surface of the jet, and for the central vortex core in the present case we complete the equations by matching the central flow to the outer z -independent line vortex flow.

5.3. Matching with z -independent outer flow

The radial expansion is not valid outside the vortex core where the flow is two-dimensional and z -independent. We match the inner and the outer solution at the drainpipe boundary $r_0(z)$ which we define by the condition

$$w(r_0(z), z) = 0, \quad (5.14)$$

and we therefore have the relation

$$r_0^2(z) = \frac{a(z)}{b(z)}. \quad (5.15)$$

At the drainpipe boundary we require that the velocity and the pressure are continuous. We assume that the bottom Ekman layer outside the central down-flow region gives rise to a weak up-flow and leads to a z -independent radial in-flow. To satisfy the continuity equation we have

$$\frac{1}{2} a'(z) r_0(z) - \frac{1}{4} b'(z) r_0^3(z) = -\frac{q}{2\pi r_0(z)}, \quad (5.16)$$

where q is the radial flow-rate per height through the drainpipe boundary. Similarly the azimuthal velocity of the inner solution is required to match the outer line vortex at the drainpipe boundary

$$\Omega_1(z) r_0(z) + \Omega_3(z) r_0^3(z) = \frac{\Gamma}{2\pi r_0(z)}, \quad (5.17)$$

and the pressure is required to be continuous at the drainpipe boundary

$$p_0(z) + p_2(z) r_0^2(z) = g(H - z) - \frac{\Gamma^2}{8\pi^2 r_0^2(z)}. \quad (5.18)$$

All in all we have 6 unknown functions, the three governing equations (5.11) – (5.13), and the three matching conditions (5.16) – (5.18). We eliminate Ω_3 , p_0 , and p_2 , and reduce the model to the three equations

$$a \Omega_1' - \left(\frac{8\nu b}{a} + a' \right) \Omega_1 + \frac{4\nu \Gamma b^2}{\pi a^2} = 0, \quad (5.19)$$

$$(a^2)' - 8\nu b - \frac{\Gamma^2}{4\pi^2} \left(\frac{b}{a} \right)' - \left(\frac{\Omega_1^2 a}{b} \right)' = 0, \quad (5.20)$$

$$\frac{1}{2} a' \frac{a}{b} - \frac{1}{4} b' \left(\frac{a}{b} \right)^2 = -\frac{q}{2\pi}. \quad (5.21)$$

5.4. *The central swirl parameter*

The three ordinary differential equations form a complete system of equations, which can be reduced to a single 1st order differential equation. The first step in deriving this result is to rewrite the continuity equation (5.21) in the form

$$\left(\frac{a^2}{b} \right)' = -\frac{2}{\pi} q. \quad (5.22)$$

We integrate the equation directly and obtain

$$\frac{a^2}{b} = \frac{2}{\pi} \left[T + Q \left(1 - \frac{z}{H} \right) \right], \quad (5.23)$$

where H is the central depth of the fluid, $Q \equiv Hq$ the radial flow-rate through the drainpipe boundary, and T a constant of integration which models the flow-rate supplied by the region above the drainpipe, including the top surface layer.

An increase in the central down-flow velocity a is associated with an increase in the central rotation rate Ω_1 due to vortex stretching. Equation (5.19) can be rewritten

$$a^2 \left(\frac{\Omega_1}{a} \right)' - 8\nu \left(\frac{b \Omega_1}{a} - \frac{\Gamma b^2}{2\pi a^2} \right) = 0, \quad (5.24)$$

and we thus observe that the central swirl parameter Ω_1/a is conserved if the viscous term is neglected. Equation (5.24) is identical to the linear 1st order differential equation

$$\left(\frac{\Omega_1}{a}\right)' - 8\nu \left(\frac{b}{a^2} \frac{\Omega_1}{a} - \frac{\Gamma b^2}{2\pi a^4}\right) = 0, \quad (5.25)$$

which we solve analytically using the expression for the flow-rate (5.23). We thus reduce the three 1st order equations to a single 1st order differential equation by integrating both the matching condition for the radial velocity and the azimuthal equation analytically.

For $q \neq 0$ and $q \neq 4\pi\nu$ we find the general solution

$$\frac{\Omega_1}{a} = \frac{\Gamma}{4[T + Q(1 - z/H)](1 - \text{Re}_r)} + C_1 \left[T + Q\left(1 - \frac{z}{H}\right)\right]^{-1/\text{Re}_r}, \quad (5.26)$$

where C_1 is an integration constant linked to the boundary condition $\Omega_1(0)$ by

$$\Omega_1(0) = \frac{1}{R^2} \left[\frac{\Gamma}{2\pi(1 - \text{Re}_r)} + \frac{2C_1}{\pi} (Q + T)^{1-1/\text{Re}_r} \right], \quad (5.27)$$

and where we define the radial Reynolds number $\text{Re}_r = q/4\pi\nu$.

5.5. Numerical solution of the axial equation

We rewrite the axial equation (5.20) as an equation for a alone using the analytic results for the flow-rate, a^2/b , and the central swirl parameter, Ω_1/a . We change variables from z to $y = T + Q(1 - z/H)$, and for $\text{Re}_r \neq 0$ and $\text{Re}_r \neq 1$ we find the equation

$$(a^2)' + \frac{a^2}{\text{Re}_r y} - \frac{\Gamma^2}{8\pi} \left(\frac{a}{y}\right)' - \frac{2}{\pi} \left[\left[\frac{\Gamma}{4(1 - \text{Re}_r)y} + C_1 y^{-1/\text{Re}_r} \right]^2 y a \right]' = 0, \quad (5.28)$$

where the derivatives are taken with respect to y . The boundary conditions for $a(z)$ and $b(z)$ at $z = 0$ are given in terms of the drain-hole radius and the total flow-rate

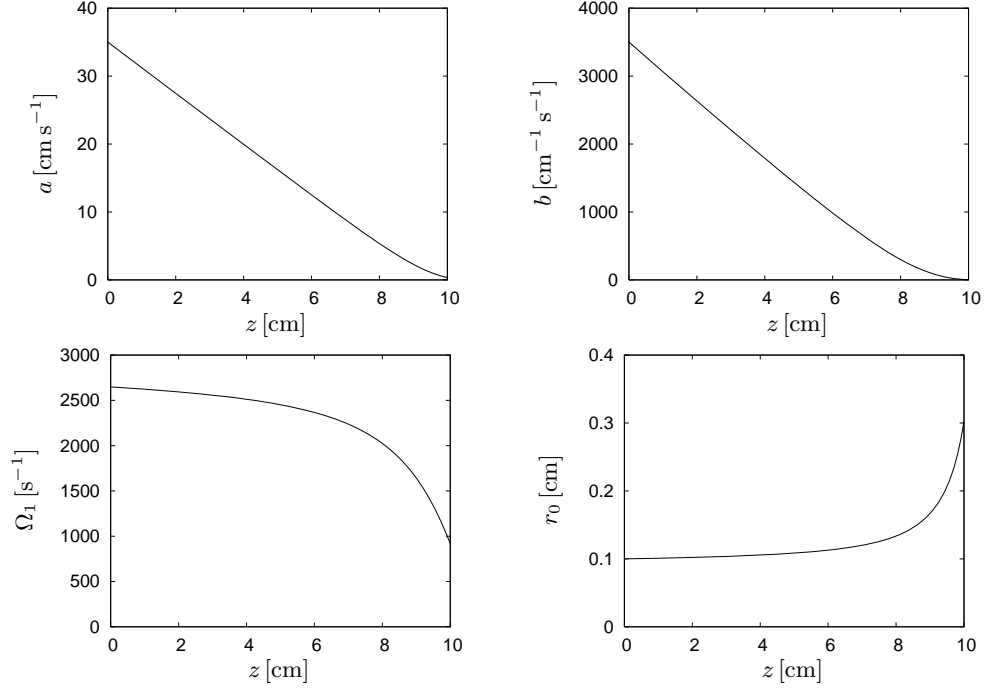


FIGURE 10. Numerical solution of equation (5.28) with $R = 0.1$ cm, $H = 10.0$ cm, $\Gamma/2\pi = 15.0$ cm² s⁻¹, $\nu = 0.01$ cm² s⁻¹, $Q = 0.5$ cm³ s⁻¹, $T = 0.05$ cm³ s⁻¹, and $C_1 = 1.0$ in CGS unit. The parameters give $\text{Re}_r = 5/4\pi \approx 0.4$. The axial velocity functions a and b , the angular velocity Ω_1 , and the drainpipe radius r_0 are shown as functions of z .

$$\frac{a(z=0)}{b(z=0)} = R^2, \quad \frac{a^2(z=0)}{b(z=0)} = \frac{2}{\pi} (T + Q), \quad (5.29)$$

and we therefore have the boundary condition

$$a(z=0) = \frac{2(T + Q)}{\pi R^2}. \quad (5.30)$$

Figure 10 shows a typical numerical solution of the drainpipe model (5.28). The axial velocity functions a and b are approximately linear in a large z -range, whereas the angular velocity Ω_1 varies slowly and is almost constant in the same z -range. The drainpipe radius r_0 is similarly almost constant except at the top where the drainpipe expands.

6. Lundgren's model

To model the free surface of the bathtub vortex we need equations which include the free surface height and satisfy the kinematic and the dynamical boundary condition at the free surface. In the following we outline the model developed by Lundgren (1985) of the free surface bathtub vortex in a rotating cylindrical container with a drain-hole. Lundgren derived a system of two coupled ordinary differential equations for the azimuthal velocity and the surface height under the assumption of a small central down-flow velocity

$$W^2 \ll 2gH, \quad (6.1)$$

and a small global Rossby number

$$\text{Ro} = \frac{W}{H\Omega} \ll 1, \quad (6.2)$$

see Lundgren (1985) equations (4.1), (4.15), and (4.18). In the bathtub vortex experiment we have $\text{Ro} \approx 10$, and we do not satisfy equation (6.2). However, we have $\text{Ro}_C \approx 0.01$. We therefore satisfy the weaker but sufficient condition (5.1) and the approximation of the radial equation (5.3) is applicable. The outflow in the experiment is driven by gravity, and we thus have that $W^2 \approx 2gH$ from Torricelli's theorem. The assumption of a small central down-flow velocity (6.1) is thus not satisfied in the experiment, and we should expect corrections to hydrostatic pressure. However, the vertical velocities close to the free surface are considerably smaller than the free fall velocity at the drain-hole, since we have a stagnation point at the tip and the vertical velocity increases downward.

6.1. Governing equations and boundary conditions

We assume that the central Rossby number is small, see equation (5.1), and apply the vertical boundary layer approximation (5.3) – (5.5) to model the central free surface

vortex flow. The flow is required to satisfy the kinematic boundary condition at the free surface which expresses that the flow is parallel to the surface:

$$\frac{dh}{dr} = \frac{w}{u} \quad \text{at} \quad z = h(r) , \quad (6.3)$$

where we use $h(r)$ to denote the height of the free surface. There is also a dynamical boundary condition at the free surface which expresses that the force terms at the surface must balance the pressure force from the air which acts perpendicular to the surface, see Batchelor (1967). In this section we neglect the viscous terms in the dynamical boundary condition and we only require that the pressure is constant at the surface.

6.2. *Lundgren's differential equations*

The axial Navier-Stokes equation (5.5) simplifies considerably if the downward velocities are small compared with the free fall velocity, i.e., if the condition (6.1) is satisfied. We neglect the nonlinear terms in the axial Navier-Stokes equation and in the following we shall in addition assume that the viscous terms in the axial equation are also negligible. The axial equation thus reduces to

$$0 = -\frac{1}{\rho} \frac{\partial p}{\partial z} - g . \quad (6.4)$$

This equation is directly integrated and to satisfy the dynamical boundary condition at the free surface we require that the pressure is constant at the surface. We thus obtain the standard equation for hydrostatic pressure

$$p(r, z) = \rho g [h(r) - z] . \quad (6.5)$$

The radial Navier-Stokes equation (5.3) therefore reduces to the balance between the hydrostatic pressure gradient and the centrifugal term

$$\frac{v^2}{r} = g \frac{dh}{dr} . \quad (6.6)$$

This equation makes it evident that the azimuthal velocity, v , is independent of the height z and thus a function of r only. Terms like $w \partial v / \partial z$ in the azimuthal Navier-Stokes equation (5.4) thus vanish and the equation reduces to the ordinary differential equation

$$u \left(\frac{dv}{dr} + \frac{v}{r} \right) = \nu \left(\frac{d^2v}{dr^2} + \frac{1}{r} \frac{dv}{dr} - \frac{v}{r^2} \right) , \quad (6.7)$$

from which it follows that the radial velocity is also independent of height. The three Navier-Stokes equations have thus been reduced to the two ordinary differential equations (6.6) and (6.7) which involve the three unknown functions u , v , and h .

The flow must in addition satisfy the continuity equation (5.6) and the kinematic boundary condition at the free surface (6.3). The fact that u is independent of z has the important consequence that w is linear in z . This result follows from the continuity equation (5.6) which thus can be written

$$\frac{1}{r} \frac{d(ru)}{dr} + \frac{w(z=h) - w(z=0)}{h} = 0 , \quad (6.8)$$

where $w(z=0)$ and $w(z=h)$ are the vertical velocities at the bottom and at the surface, respectively. We shall take $w(z=0)$ to be the vertical velocity immediately above the Ekman layer, and the Ekman pumping velocity thus puts an important constraint on the free surface flow above. It follows that $w(z=h)$ can be eliminated from the continuity equation using the kinematic boundary condition (6.3) and we obtain the equation

$$\frac{1}{r} \frac{d(hru)}{dr} = w(z=0) . \quad (6.9)$$

The free surface bathtub vortex is thus modeled by the three coupled ordinary differential equations (6.6), (6.7), and (6.9). Given that the vertical velocity at the bottom $w(z = 0)$ is known, we can obtain the product hu by integrating equation (6.9). The task is then to obtain h and v by solving the differential equations (6.6) and (6.7).

6.3. *The vertical velocity at the bottom*

The simplest choice of $w(z = 0)$ is a plug flow inside the drainpipe and no vertical flow outside the drainpipe. For such a flow it follows directly that

$$hu = \begin{cases} -\frac{Qr}{2\pi R^2} & \text{if } r \leq R \\ -\frac{Q}{2\pi r} & \text{if } r \geq R, \end{cases} \quad (6.10)$$

where R is the radius of the down-flow region. In the model (6.10) it is assumed that the radial in-flow takes place with the flow-rate Q in the bulk of the fluid. In the bathtub vortex experiment this is, however, not the case since the main part of the radial in-flow is carried by the bottom Ekman layer. Radial in-flow above the Ekman layer only takes place in the region where up-flow from the bottom layer supplies fluid through Ekman pumping. To model $w(z = 0)$ in the experiment we therefore require that the total vertical flow-rate above the bottom Ekman layer is zero

$$0 = \int_0^\infty 2\pi r w(r, z = 0) dr. \quad (6.11)$$

The dye visualization of the bottom flow in figure 5 shows that the maximum up-flow velocity above the bottom Ekman layer is approximately 1 cm s^{-1} , and vertical velocities measured using particle tracking with a vertical light sheet suggest that the up-flow

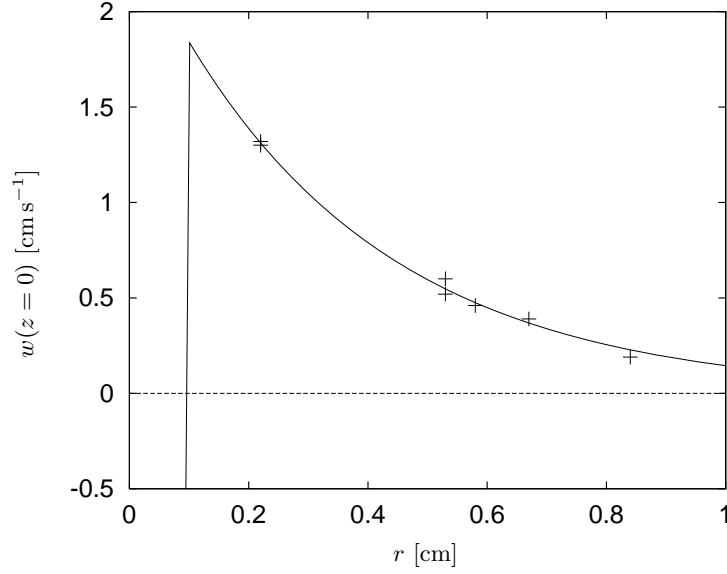


FIGURE 11. The up-flow velocities above the Ekman layer at 12 rpm. The plus signs show up-flow velocities measured 1 cm above the bottom and the solid curve a fit of the form (6.12) to the experimental data outside the drain-hole with radius 1 mm.

$w(r, z = 0)$ decreases exponentially with increasing r . Figure 11 shows measured up-flow velocities 1 cm above the bottom at 12 rpm and a theoretical fit of the form:

$$w(r, z = 0) = C \exp\left(-\frac{r}{d}\right), \quad (6.12)$$

where C and d are constants. We find $C = 2.5 \text{ cm s}^{-1}$ and $d = 3.5 \text{ mm}$ in figure 11.

Outside the down-flow region we thus use the exponential profile and for simplicity we assume that the down-flow inside the drain-hole is a plug-flow

$$w(z = 0) = \begin{cases} -\frac{Q}{\pi R^2} & \text{if } r \leq R \\ \frac{Q}{2\pi d(R+d)} \exp\left(-\frac{r-R}{d}\right) & \text{if } r \geq R. \end{cases} \quad (6.13)$$

We integrate equation (6.9) and find directly

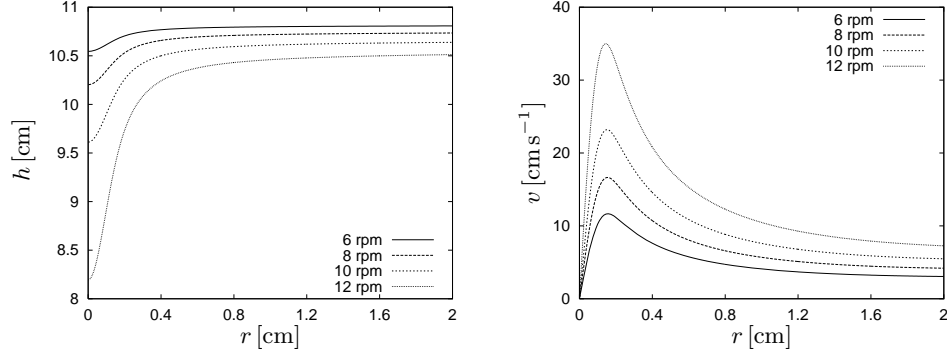


FIGURE 12. Numerical solutions of Lundgren's differential equations at rotation rates of 6 rpm, 8 rpm, 10 rpm, and 12 rpm. The surface profiles have qualitatively the same dependence on the rotation rate as the measured surface profiles at 6 rpm and 12 rpm shown in figure 2.

$$hu = \begin{cases} -\frac{Qr}{2\pi R^2} & \text{if } r \leq R \\ -\frac{Q(r+d)}{2\pi(R+d)r} \exp\left(-\frac{r-R}{d}\right) & \text{if } r \geq R. \end{cases} \quad (6.14)$$

We have only few data points for the downward velocities in the central region at 12 rpm, and we are therefore not able to determine the profile of the downward flow in detail. For simplicity we use the plug-flow profile. The actual profile is most likely in between a parabolic profile and the plug-flow profile. Our measurements show that the downward flow is not confined within a radius of 1 mm. At 12 rpm we find that $w(r = 0.13 \text{ mm}) = -84.7 \text{ cm s}^{-1}$, $w(r = 0.80 \text{ mm}) = -52.6 \text{ cm s}^{-1}$, and $w(r = 1.30 \text{ mm}) = -21.0 \text{ cm s}^{-1}$. The actual radius of the drainpipe 1 cm above the bottom is therefore between 1 mm and 2 mm, and immediately above the Ekman layer the drainpipe contracts substantially as it approaches the drain-hole.

6.4. Solutions of Lundgren's equations

We solve Lundgren's equations numerically for different values of the rotation rate and compare the numerical solutions with the experimental data at 12 rpm. We choose the

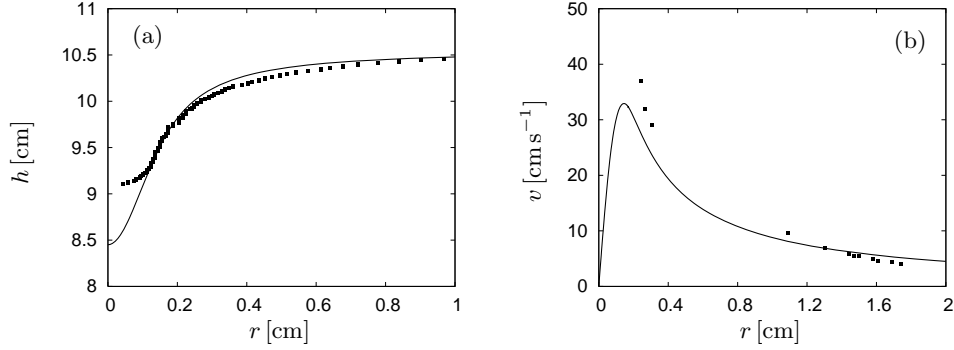


FIGURE 13. Numerical solution of Lundgren’s differential equations (solid lines) and experimental data (squares) at 12 rpm. (a) the height of the free surface and (b) the azimuthal velocity in the co-rotating reference frame. The model follows the measured surface profile outside the vortex core, but overestimates the depth of the central surface depression by about 1 cm.

vertical velocity profile (6.13) with the length scale $d = 3.5$ mm obtained from the measured profile at 12 rpm, and we use the values $R = 1.7$ mm for the radius of the down-flow region of the vertical velocity profile close to the bottom and the corresponding flow-rate $Q = 1.76$ cm³ s⁻¹. In the numerical solutions we set $g = 981$ cm s⁻², $\rho = 1.0$ g cm⁻³, and $\nu = 0.0089$ cm² s⁻¹. Figure 12 shows numerical solutions of the differential equations at 6 rpm, 8 rpm, 10 rpm, and 12 rpm. We find theoretically that the surface depression is 0.4 cm at 6 rpm and that it increases to 2.7 cm at 12 rpm. This result is in qualitative agreement with the measured surface profiles at 6 rpm and 12 rpm shown in figure 2. The azimuthal velocity increases in the central region as the rotation rate is increased and at 12 rpm the azimuthal velocities in the central region are up to 35 cm s⁻¹.

At 12 rpm we have measured both the surface profile and the azimuthal velocities in the central region. Figure 13 shows the numerical solution and the experimental data at 12 rpm. To obtain the best possible agreement with the measurements we set $R = 1.7$ mm and $Q = 1.76$ cm³ s⁻¹. The theoretical result for the surface height follows the experimental data for $r \geq 2$ mm, but overestimates the depth of the central surface

depression by approximately 1 cm. The numerical solution underestimates the measured azimuthal velocities by approximately 5 cm s^{-1} in the central vortex core. We note that there is a large difference between the surface curvature at the tip for the measurement and the numerical solution. An overestimate of the central surface depression and the curvature at the tip is to be expected since surface tension has been neglected in the model. In the following we show how to extend the model and include surface tension.

6.5. *The governing equations with surface tension*

The dynamical boundary condition at the free surface is modified due to surface tension and thus there is a correction to the hydrostatic pressure term in the approximation of the radial Navier-Stokes equation

$$\frac{v^2}{r} = g \frac{dh}{dr} - \frac{\alpha}{\rho} \frac{d\kappa}{dr}, \quad (6.15)$$

where α is the surface tension and κ is the curvature of the surface

$$\kappa = \frac{h'}{r[1 + (h')^2]^{1/2}} + \frac{h''}{[1 + (h')^2]^{3/2}}. \quad (6.16)$$

The relative importance of the hydrostatic pressure and the Laplace pressure due to surface tension is conveniently described using the capillary length

$$l = \sqrt{\frac{\alpha}{g\rho}}. \quad (6.17)$$

Surface tension is important if the radius of curvature of the surface is smaller than or comparable with the capillary length. By integrating the radial Navier-Stokes equation (6.15) we obtain

$$h(r) - h(0) = \frac{1}{g} \int_0^r \frac{v^2}{r'} dr' + l^2 [\kappa(r) - \kappa(0)], \quad (6.18)$$

from which it follows that the depth of the central surface depression is

$$h(\infty) - h(0) = \frac{1}{g} \int_0^\infty \frac{v^2}{r} dr - l^2 \kappa(0), \quad (6.19)$$

where we have assumed that the curvature is zero at infinity. With a given azimuthal velocity profile we thus find that the depth of the central depression is reduced due to surface tension and that the correction term is proportional to the central curvature.

6.6. Surface tension effects for the bathtub vortex

The surface tension of a clean air-water interface is 72.0 gs^{-2} at 25°C , and thus the capillary length is $l = 0.271 \text{ cm}$ in this case (see Kaye & Laby (1973)). We measured $\alpha = 65 \text{ gs}^{-2}$ for the air-water interface in our experiment. A priori we therefore expect that surface tension plays an important role for the detailed shape of the surface of the bathtub vortex in the central region. To estimate the effect of surface tension on the free surface height we fit the central part of the surface profile by the polynomial

$$h(r) = h_0 + \frac{1}{2} h_2 r^2 + \frac{1}{4} h_4 r^4, \quad (6.20)$$

and we thereby obtain the central curvature $\kappa(0) = 2 h_2$. A fit of the form (6.20) to the measured surface profile at 12 rpm for $r \leq 1 \text{ mm}$ gave $h_2 = 11 \text{ cm}^{-1}$, and we therefore estimate that surface tension reduces the central surface dip by approximately 1.6 cm at 12 rpm. The overestimate of the depth of the central surface depression can thus be explained by the neglect of surface tension in the model.

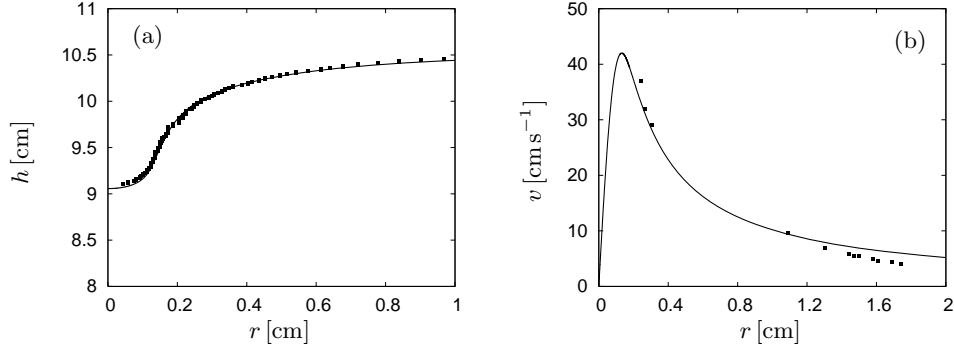


FIGURE 14. Numerical solution of Lundgren's differential equations with surface tension (solid lines) and experimental data (squares) at 12 rpm. (a) the height of the free surface and (b) the azimuthal velocity in the co-rotating reference frame. Both the surface profile and the azimuthal velocity are described well when surface tension is included in the model.

6.7. Lundgren's model with surface tension

The differential equations for the azimuthal velocity and the surface height are more complicated to solve numerically when surface tension is included. The derivative of the curvature in equation (6.15) involves the third derivative of the surface height and the radial equation is therefore of third order in comparison with the 1st order equation (6.6) for the problem without surface tension. We have solved the differential equations numerically using a finite difference approach to the two point boundary value problem. Figure 14 shows the solution of Lundgren's model with surface tension effects included. To obtain the best possible agreement with the measurements we set $R = 0.16$ cm and $Q = 1.79$ cm³ s⁻¹. The solution with surface tension describes both the measured surface depression and azimuthal velocities well. The model with surface tension captures the curvature of the surface profile at the tip of the surface depression well, and we note that this was not possible without surface tension as shown in figure 13(a).

7. Conclusions

We presented an experimental and theoretical investigation of the time-independent bathtub vortex in a rotating cylindrical container with a small drain-hole at the center of the bottom. Experimentally we found an intense vortex, a strong central surface depression above the drain-hole, and a complex flow structure with four characteristic flow regions, i.e., the geostrophic bulk, the bottom Ekman boundary layer, the surface boundary layer, and the central vortex core with localized axial down-flow.

The central vortex core is surrounded by a bulk region with a two-dimensional line vortex flow which is independent of height. At the container bottom an Ekman boundary layer is formed which gives rise to up-flow outside the central down-flow region. The main part of the radial inflow takes place in the bottom Ekman layer, which thereby connects the flow-rate and the strength of the line vortex. We found good agreement between our measurements and linear Ekman theory, and we described the nonlinear properties of the bottom Ekman layer theoretically using an averaging technique with a non self-similar profile with separate length scales for the decay and the oscillations, respectively. We predicted that the boundary layer thickness is smaller and that the central up-flow is reduced in comparison with the results of linear Ekman theory in the vortex core where the local Rossby number is large. However, experimentally we did not resolve the boundary layer structure sufficiently to test the predictions.

We modeled the central down-flow above the drain-hole with a radial expansion method in which we matched an inner viscous solution to an outer height independent line vortex. Analytically we reduced the model to a single 1st order differential equation and numerically we found that the axial velocity typically depends linearly on height whereas the azimuthal velocity is almost independent of height. The radial expansion method can be adapted to model a bathtub vortex with the free surface extending down to the drain-

hole. However, the parabolic ansatz for the down-flow does not allow for a description of a flow with a central stagnation point on the axis of symmetry. To model the flow close to such a point we must expand w to 4th order

$$w(r, z) = -a(z) + b(z)r^2 + c(z)r^4, \quad (7.1)$$

and to consider the governing equations to the 2nd lowest order in r . The function a is equal to zero at the stagnation point, whereas b and c are not restricted to have any specific values there. Above the stagnation point a is negative whereas a is positive below the stagnation point where we expect that the down-flow is well described by a parabolic profile. At the same time the vertical boundary layer approximation is not applicable close to the stagnation point, since the vertical and the radial velocities are comparable there. To model flows with a finite surface depression there are thus several things which complicate the calculations, but the 4th order down-flow profile allows for a description of the topology of the flow around the tip of the surface depression.

To model the shape of the surface depression we applied Lundgren's model of the bathtub vortex with a free surface and compared numerical solutions of the model with our experimental data on the surface profile and the vertical and azimuthal velocities. We found that the numerical solutions were in qualitative agreement with the measurements and showed a similar dependence on the rotation rate of the container as the measured surface profiles. We discussed the importance of surface tension and showed how to include surface tension corrections in Lundgren's differential equations. We found that the measured velocities and surface profiles were well described quantitatively by the model when Ekman up-flow and surface tension effects were included.

REFERENCES

- ANDERSEN, A., BOHR, T., STENUM, B., JUUL RASMUSSEN, J. & LAUTRUP, B. 2003 Anatomy of a Bathtub Vortex. *Phys. Rev. Lett.* **91**, 104502.
- ANDERSEN, A., LAUTRUP, B. & BOHR, T. 2003 An averaging method for nonlinear laminar Ekman layers. *J. Fluid Mech.* **487**, 81-90. Corrigendum: *J. Fluid Mech.* **493**, 379.
- BATCHELOR, G. K. 1967 *An Introduction to Fluid Dynamics*. Cambridge University Press.
- DONALDSON, C. DUP. & SULLIVAN, R. D. 1960 Behaviour of solutions of the Navier-Stokes equations for a complete class of three-dimensional viscous vortices, *Proc. Heat Transfer and Fluid Mechanics Institute, Stanford University*, 16.
- EGGERS, J. & BRENNER, M. P. 2000 Spinning jets, *Proceedings of the IUTAM Symposium on Nonlinear Waves in Multi-Phase Flow*. Kluwer, Dordrecht.
- EINSTEIN, H. A. & LI, H. 1951 Steady vortex flow in a real fluid, *Proc. Heat Transfer and Fluid Mechanics Institute, Stanford University*, 33-43.
- FEYNMAN, R. P., LEIGHTON, R. B. & SANDS, M. 1965 *The Feynman Lectures on Physics*. Addison Wesley, Reading, Massachusetts.
- GREENSPAN, H. P. 1968 *The theory of rotating fluids*. Cambridge University Press.
- KÁRMÁN, T. VON 1921 Über laminare und turbulente Reibung. *Z. angew. Math. Mech.* **1**, 233-252.
- KAWAKUBO, T., TSUCHIYA, Y., SUGAYA, M. & MATSUMURA, K. 1978 Formation of a vortex around a sink: A kind of phase transition in a nonequilibrium open system. *Phys. Lett. A* **68**, 65-66.
- KAYE, G. W. C & LABY, T. H. 1973 *Tables of Physical and Chemical Constants, 14th Edition*. Longman, London.
- LAMB, H. 1945 *Hydrodynamics*. Dover Publications, New York.
- LEWELLEN, W. S. 1962 A solution for three-dimensional vortex flows with strong circulation. *J. Fluid Mech.* **14**, 420-32.
- LUGT, H. J. 1995 *Vortex Flow in Nature and Technology*. Krieger.
- LUNDGREN, T. S. 1985 The vortical flow above the drain-hole in a rotating vessel. *J. Fluid Mech.* **155**, 381-412.

- 42 *A. Andersen, T. Bohr, B. Stenum, J. Juul Rasmussen and B. Lautrup*
- MORY, M. & YURCHENKO, N. 1993 Vortex generation by suction in a rotating tank. *Eur. J. Mech., B/Fluids* **12**, 729-47.
- OWEN, J. M., PINCOMBE, J. R. & ROGERS, R. H. 1985 Source-sink flow inside a rotating cylindrical cavity. *J. Fluid Mech.* **155**, 233-265.
- POHLHAUSEN, K. 1921 Zur näherungsweise Integration der Differentialgleichung der laminaren Grenzschicht. *Z. angew. Math. Mech.* **1**, 252-268.
- SHAPIRO, A. H. 1962 Bath-Tub Vortex. *Nature* **196** 1080-81.
- TREFETHEN, L. M., BILGER, R. W., FINK, P. T., LUXTON, R. E. & TANNER, R. I. 1965 The Bath-Tub Vortex in the Southern Hemisphere. *Nature* **207** 1084-85.